

Transparent and Flexible Supercapacitors with Networked Electrodes

S. Kiruthika, Chaitali Sow, and G. U. Kulkarni*

Transparent and flexible energy storage devices have received immense attention due to their suitability for innovative electronics and displays. However, it remains a great challenge to fabricate devices with high storage capacity and high degree of transmittance. This study describes a simple process for fabrication of supercapacitors with $\approx 75\%$ of visible transparency and areal capacitance of $\approx 3 \text{ mF cm}^{-2}$ with high stability tested over 5000 cycles of charging and discharging. The electrodes consist of Au wire networks obtained by a simple crackle template method which are coated with MnO_2 nanostructures by electrodeposition process. Importantly, the membrane separator itself is employed as substrate to bring in the desired transparency and light weight while additionally exploiting its porous nature in enhancing the interaction of electrolyte with the active material from both sides of the substrate, thereby enhancing the storage capacity. The method opens up new ways for fabricating transparent devices.

1. Introduction

Light weight and flexible energy storage devices have attracted a great attention mainly due to the increasing demand for integration in devices such as portable personal electronics. Among them, supercapacitors have become increasingly popular as they provide higher power densities than the lithium ion batteries and higher energy densities than electrolytic capacitors along with many additional advantages such as long cycle life, fast charging–discharging rates as well as enhanced safety.^[1,2] The application area is wide—from pulse power systems to electric vehicles—where rapid energy

release on demand is crucial.^[3] Typically, a supercapacitor is composed of a set of current collectors made of a chosen electrode material, an electrolyte and a separator. In contrast to metal strips current collectors such as copper, stainless steel, and nickel foils, conducting thin films deposited on polymer (polyethylene terephthalate (PET)) or paper substrates afford light weight.^[4] Light-weight supercapacitors have been fabricated on various paper substrates, including photocopier paper, commercial separator membrane, lens wiping papers, etc.^[5–10] Thus, fabricated devices possess an integrated structure, in which the separator membrane is made to host the two electrodes on both sides. Besides being light weight, these devices provide high areal capacitance and are usually stable toward many charge storage cycles.^[5] However, while integrating device on a sheet of paper, the micrometer-sized pores present in the cellulose matrix may lead to short circuiting. This issue is resolved by coating polyvinylidene fluoride (PVDF) or graphene from pencil trace on both sides of porous paper membranes before loading active materials.^[7–9] This work focuses on the fabrication of a light weight supercapacitor from quite a different approach.

Extensive research is being done to incorporate aesthetic properties such as transparency, flexibility, and wearability to the intrinsic performance of the futuristic supercapacitors.^[11,12] The supercapacitors reported in the literature are largely opaque mainly due to nontransparency of either

S. Kiruthika, C. Sow, Prof. G. U. Kulkarni
Chemistry and Physics of Materials Unit and Thematic
Unit of Excellence in Nanochemistry
Jawaharlal Nehru Centre for Advanced
Scientific Research
Jakkur P.O., Bangalore 560064, India
E-mail: guk@cens.res.in

Prof. G. U. Kulkarni
Centre for Nano and Soft Matter Sciences
Jalahalli, Bangalore 560013, India



The ORCID identification number(s) for the author(s) of this article can be found under <https://doi.org/10.1002/sml.201701906>.



DOI: 10.1002/sml.201701906

the substrate or the active material.^[5,7,8] Recent efforts have focused on developing entirely transparent devices by incorporating transparent current collectors and thin layers of active materials. Due to several drawbacks of traditional indium tin oxide (ITO) transparent electrodes such as scarcity, high processing cost, limited chemical resistance as well as lack of flexibility, alternative electrodes consisting of graphene, carbon nanotubes (CNTs), metal nanowires or metal meshes are being pursued.^[13–18] As regards the transparency of the active layer, reducing the thickness alone may not be helpful; the areal capacitance may get adversely affected.^[11] Recently, there have been significant efforts dedicated toward the fabrication of transparent supercapacitors with creative new designs to enable some transparency in the device.^[19–21] In an instance, Zhi and co-workers, employing a nanosphere lithography process, produced Au/MnO₂ core-shell mesh electrodes which yielded 48% transparency in the device with an areal capacitance of 4.7 mF cm⁻² in three-electrode configuration.^[22] However, the lithography method is inherently unsuitable for large area device fabrication and mass production. In another report, free-standing transparent graphene paper was used as an effective active material for energy storage.^[23] Despite their flexibility and high efficiency for charge storage (3 mF cm⁻²), the obtained transparency of the device was <50%. On the other hand, the supercapacitor with the transparency of 75% has been achieved with ≈2 nm thick graphene as an active layer. However, the areal-specific capacitance of the device is only 0.1 mF cm⁻².^[11] Thus, there appears to be a trade-off between the transparency and energy storing capability of the device. In this work, a lightweight flexible device has been fabricated with an additional attribute of visible transparency without in any way compromising the device performance. Specifically, over an Au mesh transparent current collector hosted on membrane separator, pseudocapacitive MnO₂ nanostructures were grown. The fabricated energy storage devices were highly flexible, light weight, and transparent (≈75%) with typical areal capacitance of ≈3 mF cm⁻².

2. Results and Discussion

Schematic of the fabrication process to prepare an Au/MnO₂ core-shell wire network is presented in **Figure 1a**. The transparent Au wire network-based current collector was obtained using the crackle template method pioneered in the laboratory.^[24–30] Initially, a highly interconnected crackle template with crack widths in the range of 10–20 μm (see Figure S1 in the Supporting Information) was obtained over the separator substrate. The networks were highly interconnected over a large area and down to the substrate as seen in optical micrographs (see Figure S1a,b in the Supporting Information). The crackles were down to the separator and devoid of any crackle precursor and can be readily used as a template for metal deposition. After Au deposition and removal of the template, Au wire mesh (<5 Ω □⁻¹, 86% transmittance) with seamless junctions was obtained on the substrate (see Figure S2 in the Supporting Information). The optoelectronic properties of the Au mesh electrode could be further varied by modulating

the density, width, and thickness of the metal mesh.^[27] The Au wire networks were coated with high surface area MnO₂ nanostructures by an electrodeposition process. The low- and high-resolution scanning electron microscope (SEM) images of the Au/MnO₂ deposited for 60 min (henceforth, Au/MnO₂ (60 min)) core-shell networks are shown in Figure 1b,c, respectively. From the elemental mapping, it is clear that the Au wire mesh is uniformly coated with MnO₂ shell (see Figure S3 in the Supporting Information). Unlike metal nanowire networks, where issues arising out of crossbar junctions and agglomerations are highly troublesome for devices, the Au/MnO₂ network has a low surface roughness due to the in-plane arrangement as shown in Figure 1d. Complete encapsulation of the Au core by MnO₂ is evidenced from the side view SEM images in Figure 1e,f (see also Figure S4 in the Supporting Information). The highly porous and spiky nature of MnO₂ is supported from the SEM and transmission electron microscopic (TEM) images in Figure 1f,g, respectively. Furthermore, MnO₂ deposition improves the wettability of Na₂SO₄ (an electrolyte) and reduces the contact angle (48°) (Figure 1h,i). The hydrophilic nature of the electrode is highly desirable in this context for fast access of the ions to the interface between the electrode and the electrolyte. The chemical compositions and the oxidation states of Mn in the Au/MnO₂ wire network were analyzed using X-ray photoelectron spectroscopy (XPS) studies. The survey XPS spectrum (see Figure S5 in the Supporting Information) shows the presence of Mn, O, and C elements as major peaks. The carbon content comes from the polypropylene substrate (separator) as Au/MnO₂ is present as network structure with a 2D fill factor of ≈20%. While such a structure enables electrolyte interaction on the sidewalls of the wires carrying the MnO₂ nanostructure, it does expose the substrate in the middle polygonal areas, contributing to C 1s signal. The core-level XPS spectrum of Mn 2p is shown in Figure 1j. The peaks located at 642.2 and 653.9 eV correspond to Mn 2p_{3/2} and Mn 2p_{1/2} electrons, respectively, suggest the presence of Mn⁴⁺ in the obtained MnO₂ nanostructures. In addition, the spin energy separation of 11.8 eV between the binding energies of Mn 2p levels matches well with that reported for MnO₂.^[31] The O 1s deconvolution leads to three features at ≈529.8, 531.2, and 533 eV corresponding to Mn–O–Mn of oxides, Mn–O–H of hydroxides and H–O–H of residual water, respectively (Figure 1k).^[32]

A photograph of the fabricated Au/MnO₂ electrode on the separator is shown in **Figure 2a** with the transmittance spectrum in Figure 2b. As seen from the spectrum, the transparency is ≈81% at 550 nm, which is not significantly less compared to that of bare Au mesh (≈86%) in spite of the growth of MnO₂ on top. The optical transmittance of the assembled two-electrode supercapacitor is nearly 72% (see Figure 2b), which is commendable. Electrochemical performances of Au/MnO₂ wire meshes on flexible separator were measured in the two-electrode configuration in 1 M Na₂SO₄ (aq.) electrolyte. As the membrane separator itself was used as the substrate in this study, the two electrodes have been placed one over the other (see schematic in Figure 2c), rather than making them face each other with a separator in-between, as is generally done (see Figure S6 in the Supporting

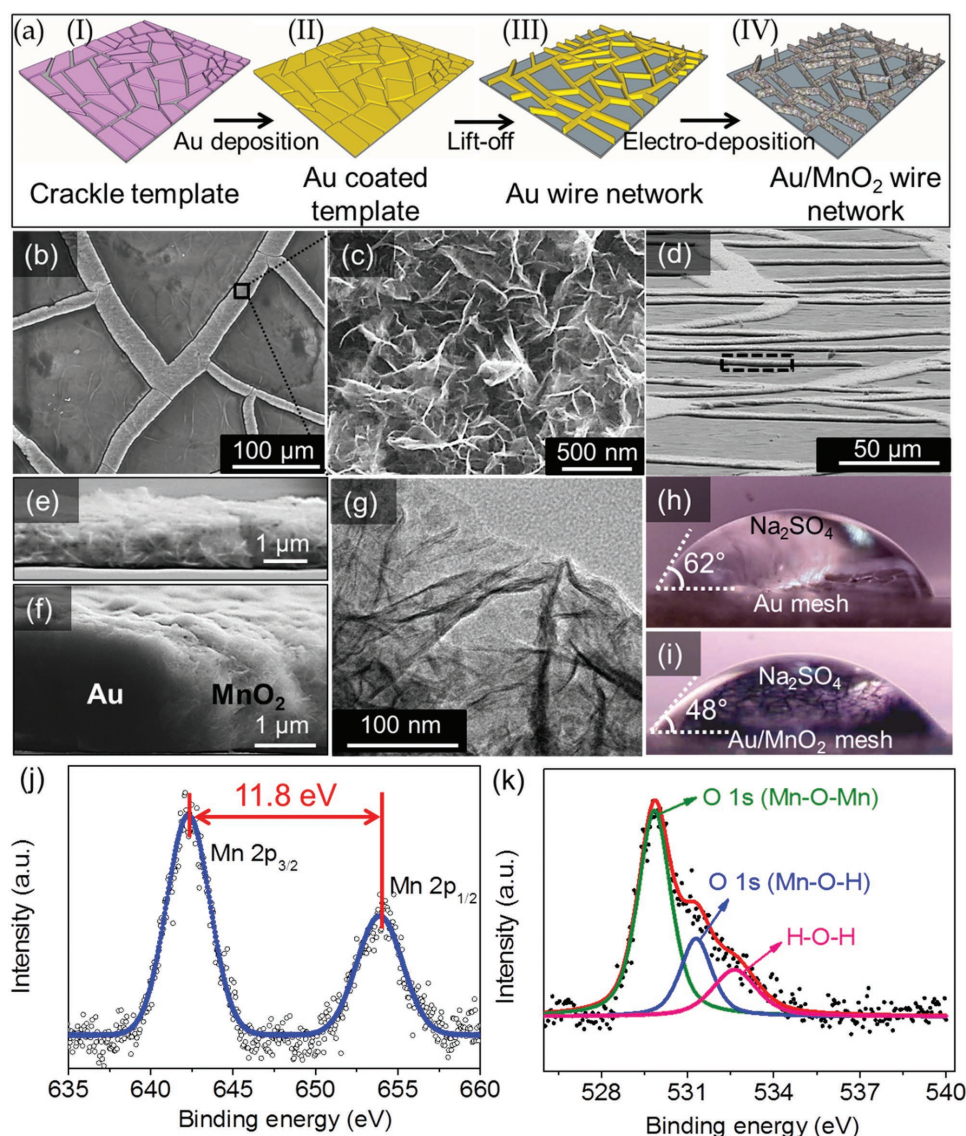


Figure 1. a) Schematic illustration for the fabrication of Au/MnO₂ wire network on the separator. In step I, the crackle template was prepared on the separator by spin coating acrylic resin-based precursor. Upon the template, Au metal was deposited by a physical evaporation method (II) followed by removal of the template to obtain highly interconnected Au wire network (III). Later, Au was decorated with MnO₂ flakes by an electrodeposition process (IV). SEM images of the fabricated Au/MnO₂ wire meshes are shown in b–f. b, c) Top views and d–f) the cross-sectional views of the Au/MnO₂ (60 min) network. The marked region in (d) is shown in (e). g) TEM image of MnO₂ flakes. Photographs of Na₂SO₄ droplets on h) Au and i) Au/MnO₂ mesh surfaces. XPS survey spectrum of j) Mn 2p and k) O 1s of Au–MnO₂ mesh on the separator substrate.

Information). The comparison of the cyclic voltammograms (CV) measured in three-electrode configuration with that from two-electrode configuration is shown in Figure S7 in the Supporting Information. The former values are quite higher as expected. Figure 2d shows the CV data for Au/MnO₂ wire meshes with different MnO₂ loadings at a scan rate of 100 mV s^{−1}, where it is observed that the Au/MnO₂ (60 min) electrodes exhibit the highest current density (0.21 mA cm^{−2}). It is important to note that capacitance from current collecting Au mesh alone is negligible (0.0005 mA cm^{−2}). Also, the current densities obtained from the device fabricated on PET substrate (Au/MnO₂(PET)/separator/Au/MnO₂ (PET)) is an order less than the device fabricated with the separator as the substrate (see Figure S8 in the Supporting Information). The CV curves of Au/MnO₂ (60 min) measured at

various scan rates from 10 to 100 mV s^{−1} exhibited nearly rectangular-shaped curves indicating the ideal capacitive behavior of the device (Figure 2e). Figure S9a–d in the Supporting Information displays the CV curves of Au/MnO₂ with different MnO₂ electrodeposition times varying from 8 to 90 min. Galvanostatic charge–discharge (CD) curves of Au/MnO₂ (60 min) transparent supercapacitors were acquired between 0 and 0.8 V potential window with various current densities ranging from 0.015 to 0.175 mA cm^{−2} (Figure 2f). CD curves are nearly triangular in shape, confirming the formation of the electrochemical double layer and efficient charge propagation across the two electrodes. The areal capacitance of these devices was calculated from both the discharging slope of CD curves (Equation (1)) measured at various current densities (Figure 2g) and from the CV curves

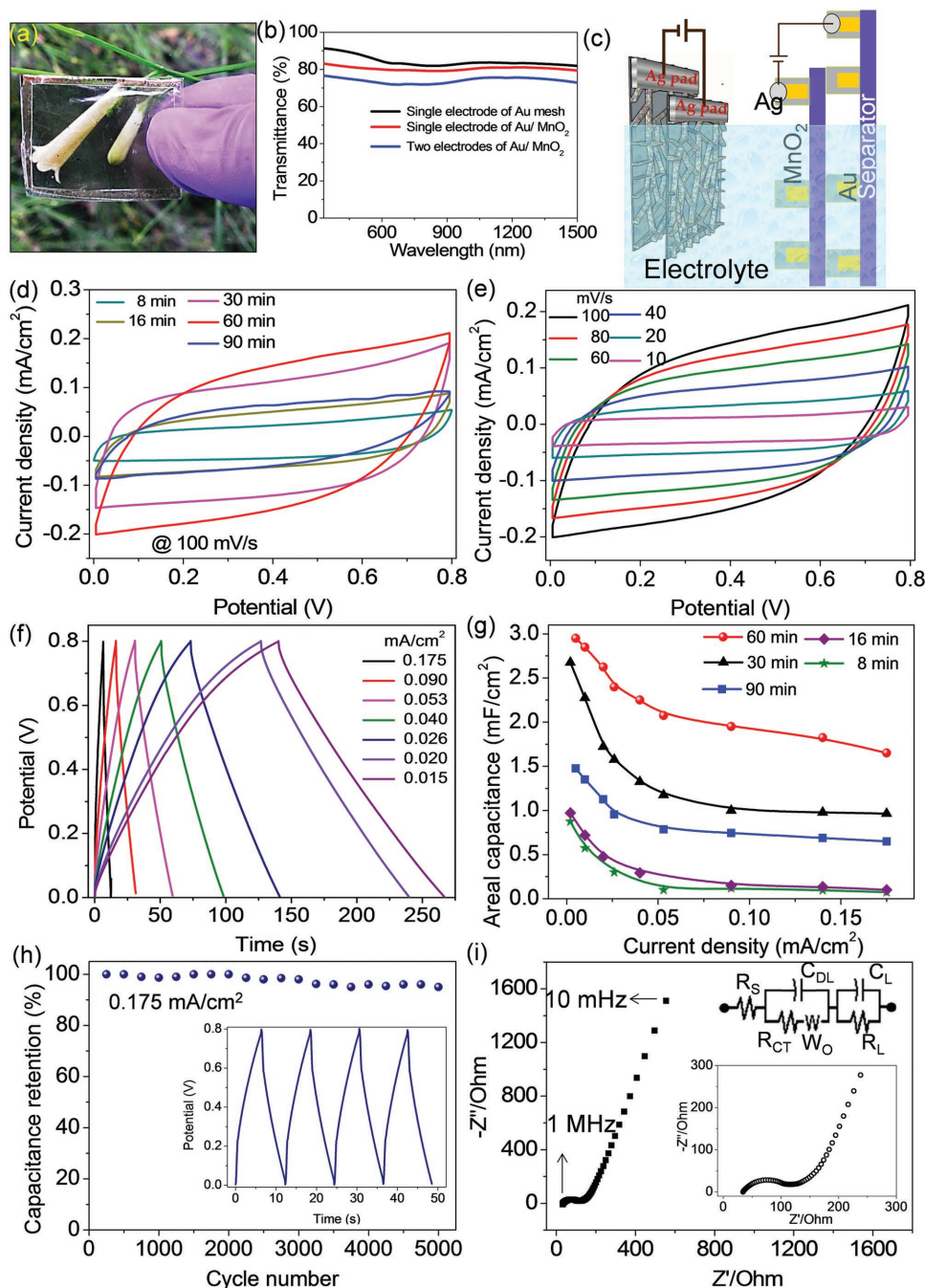


Figure 2. a) Photograph of resultant single Au/MnO₂ mesh on the separator (border laminated for stiffness). b) Transmittance spectra of Au mesh, Au/MnO₂ (60 min) mesh and assembled two Au/MnO₂ (60 min) meshes. c) Schematics of Au/MnO₂ electrode assembly/configuration. d) CV of Au/MnO₂ with different MnO₂ loading at the scan rate of 100 mV s⁻¹ in 1 M Na₂SO₄ electrolyte. CV curves at different scan rates and galvanostatic CD profile at different current densities of Au/MnO₂ (60 min) MnO₂ devices are shown in (e) and (f), respectively. g) Dependence of areal capacitance of Au/MnO₂ meshes with different MnO₂ loading on the discharging current density. h) Stability of supercapacitor for 5000 charging and discharging cycles at a current density of 0.175 mA cm⁻². Inset is the CD profile at 0.175 mA cm⁻². i) Nyquist impedance plot of Au/MnO₂ (60 min) supercapacitor. Insets are the magnified high-frequency region of impedance plot and fitted equivalent circuit where R_s is the series resistance, C_{DL} is the double-layer capacitance, R_{CT} is the charge transfer resistance, W_0 is the Warburg impedance, C_L denotes the pseudocapacitance, and R_L is the leakage resistance.

(Equation (2)) as a function of the scan rate (see Figure S10 in the Supporting Information):^[22]

$$C_{\text{areal}} = I / [-(\Delta V / \Delta t) A] \quad (1)$$

$$C_{\text{areal}} = I / s \cdot A \quad (2)$$

where C_{areal} is the areal capacitance, I is the current applied, $-(\Delta V / \Delta t)$ is the slope of the discharging curves after IR drop, A is the area of the device, and s is the scan rate in mV s⁻¹

($s = dV/dt$). Figure 2g displays the areal capacitance calculated from the CD curves. The highest areal capacitance of $\approx 3 \text{ mF cm}^{-2}$ was achieved at 0.005 mA cm^{-2} current density for Au/MnO₂ (60 min) device. It preserves 56% of the areal capacitance when the current density increases from 0.005 to 0.175 mA cm^{-2} . The areal capacitance value was found to linearly increase with MnO₂ loading up to deposition of 60 min beyond which it began to decrease. A similar trend was observed for areal capacitance values calculated from the CV curves (see Figure S10 in the Supporting Information). The areal capacitance of $1.98 \pm 0.35 \text{ mF cm}^{-2}$ (100 mV s^{-1}) was obtained from five cells fabricated with 60 min electrodeposition (see Figure S11 in the Supporting Information), evidencing the reproducibility of obtained results. The supercapacitor device (Au/MnO₂(60 min)) shows less than 5% degradation in performance after testing for 5000 CD cycles (Figure 2h). The inset in Figure 2h shows the CD profile at a current density of 0.175 mA cm^{-2} . Even after 5000 cycling test, no change in the morphology of the Au/MnO₂ network was observable (see Figure S12 in the Supporting Information). Electrochemical impedance spectroscopy (Figure 2i and Figure S13, Supporting Information) has been used as a powerful tool to understand the fundamental behavior at the electrode–electrolyte interface. Figure 2i shows the Nyquist impedance plot of Au/MnO₂ (60 min), in the frequency range, 10^{-2} to 10^6 Hz with the fitted equivalent circuit in the inset. The nearly vertical shape at low frequencies is indicative of the capacitive behavior of the device and the estimated R_s is 34.3Ω denoted from the intersection point on the real axis. Such low series resistance owes much to the highly

conducting Au mesh as well as effective charge transfer between Au and MnO₂.

Besides being highly transparent and conducting, Au/MnO₂ electrodes exhibit high flexibility and stability toward bending. Figure 3a shows the normalized resistance of Au/MnO₂ (60 min) as a function of bending cycles. The bending test was performed using a custom-designed setup in which one side was kept movable using a screw gauge with the other end fixed. Even after few hundred bending cycles (bending radius, 2.5 mm), it showed only $\approx 7\%$ rise in electrode resistance. The morphology of the electrodes was characterized after 1000 bending cycles using SEM. Even after 1000 cycles, Au–MnO₂ mesh was adhering well to the substrate as shown in Figure S14a in the Supporting Information. However, few cracks were observed on the MnO₂ layer near the junctions (see Figure S14b,c in the Supporting Information). The high-resolution SEM image clearly shows that the MnO₂ nanostructure was retained as such (Figure S14d in the Supporting Information). This explains slight increase in resistance with bending cycles (Figure 3a).

A solid-state flexible supercapacitor was also fabricated by sandwiching two Au/MnO₂ (60 min) electrodes with PVA–H₂SO₄ gel electrolyte. The transmittance of an assembled device is nearly 64% at 550 nm (see the inset in Figure 3b), which is only $\approx 7\%$ less with the introduction of the electrolyte (see Figure 2b). Furthermore, the device stability toward deformations (2.5 and 1.5 mm bending radii) (see Figure 3c and d inset) is almost as good as bare electrodes shown in Figure 3a. Even lower values of the bending radius were not possible, as no encapsulation was done on the device which

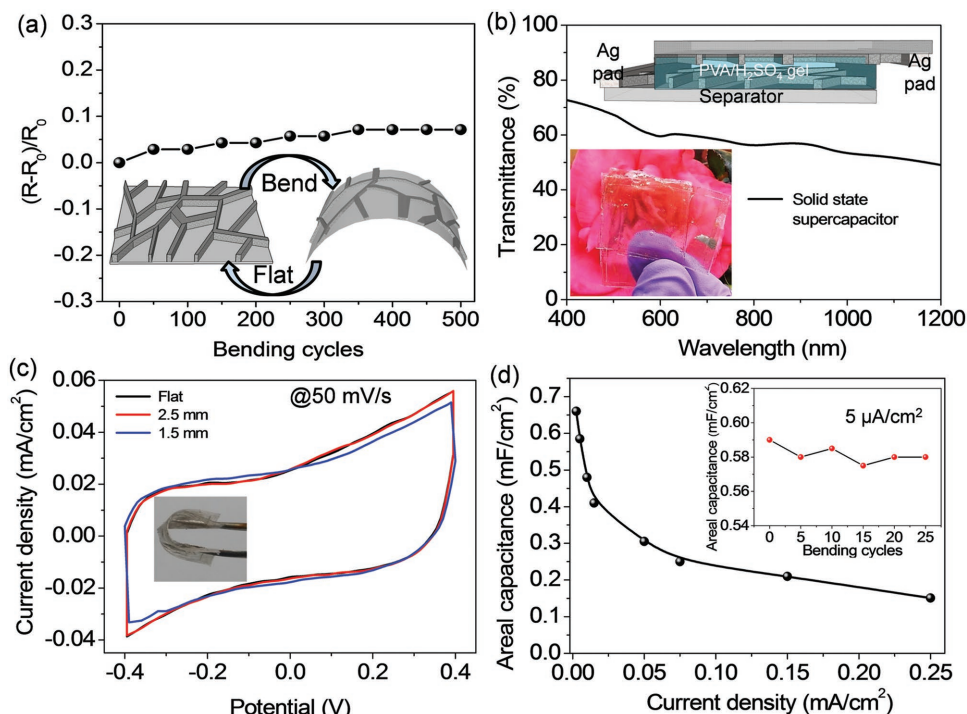


Figure 3. a) Relative change in resistance of Au/MnO₂ (60 min) electrode while bent to 2.5 mm bending radius. b) Transmittance spectrum of cross assembled solid-state supercapacitor device. Schematic of electrode alignment (top) and the photograph of the device (bottom) are shown in the inset. c) CV curves of Au–MnO₂ (60 min) solid-state supercapacitor with PVA/H₂SO₄ gel electrolyte in flat and while bent to 2.5 and 1.5 mm radii. Inset shows the photograph of a flexible supercapacitor device in bent geometry. d) Areal capacitance as a function of current densities and inset is a change in areal capacitance as a function of bending cycles.

could provide additional mechanical support. The electrochemical behavior of the solid-state device (Figure 3c) is quite comparable to that of the device with aq. electrolyte (Figure 2d). However, the specific areal capacitance of the device seems to decrease faster with increasing current density values (Figure 3d).

During the optimization stage, it has been realized that the areal capacitance value tends to decrease beyond certain MnO_2 deposition (>60 min) as well as at higher current densities (>0.05 mA cm^{-2}). Both these effects arise due to excessive resistive path for the charge carriers to reach the metal back bone (see Figure S13 in the Supporting Information). The electrolyte interaction with dense MnO_2 nanostructures may also become restrictive.^[4]

In order to achieve light-weight supercapacitors with no loss in capacitance and transmittance, fabrication of Au/MnO_2 (optimized 60 min deposition) on both sides of a separator was executed. **Figure 4a** (i–vi) schematically shows the fabrication process of Au/MnO_2 (60 min). Initially, crackle template was created on a separator (i) followed by Au deposition (ii). These process steps were repeated on another side of the separator as well (iii and iv). The Au wire networks obtained

after the removal of the templates (v) were taken further for MnO_2 deposition on both sides, in consecutive steps (vi). Here, a separator membrane besides being a substrate to hold Au/MnO_2 on both sides, it is acting as the electrical insulator between two electrodes while simultaneously allowing ion diffusion across the membrane. Thus, fabricated device is highly transparent (78%) and flexible. The clear visibility of the plant beneath the electrode illustrates its transmittance (inset of Figure 4b). The electrochemical property and resistive behavior of the fabricated devices were examined by CV and CD measurements. The CV curves were measured with different scan rates in the range of 10–100 mV s^{-1} as shown in Figure 4c. The galvanostatic CD curves at various current densities are presented in Figure 4d. Typical triangular shape of these CD curves with high symmetry indicating the high reversibility and high coulombic efficiency (ratio of discharging and charging times) of these electrodes. The areal capacitance was calculated from CD curve measured from the slope of discharge curve (Figure 4e). The maximum areal capacitance of 3.23 mF cm^{-2} was obtained at a current density of 0.005 mA cm^{-2} . As a comparison, areal capacitance calculated from two separate electrode configuration (Figure 2g)

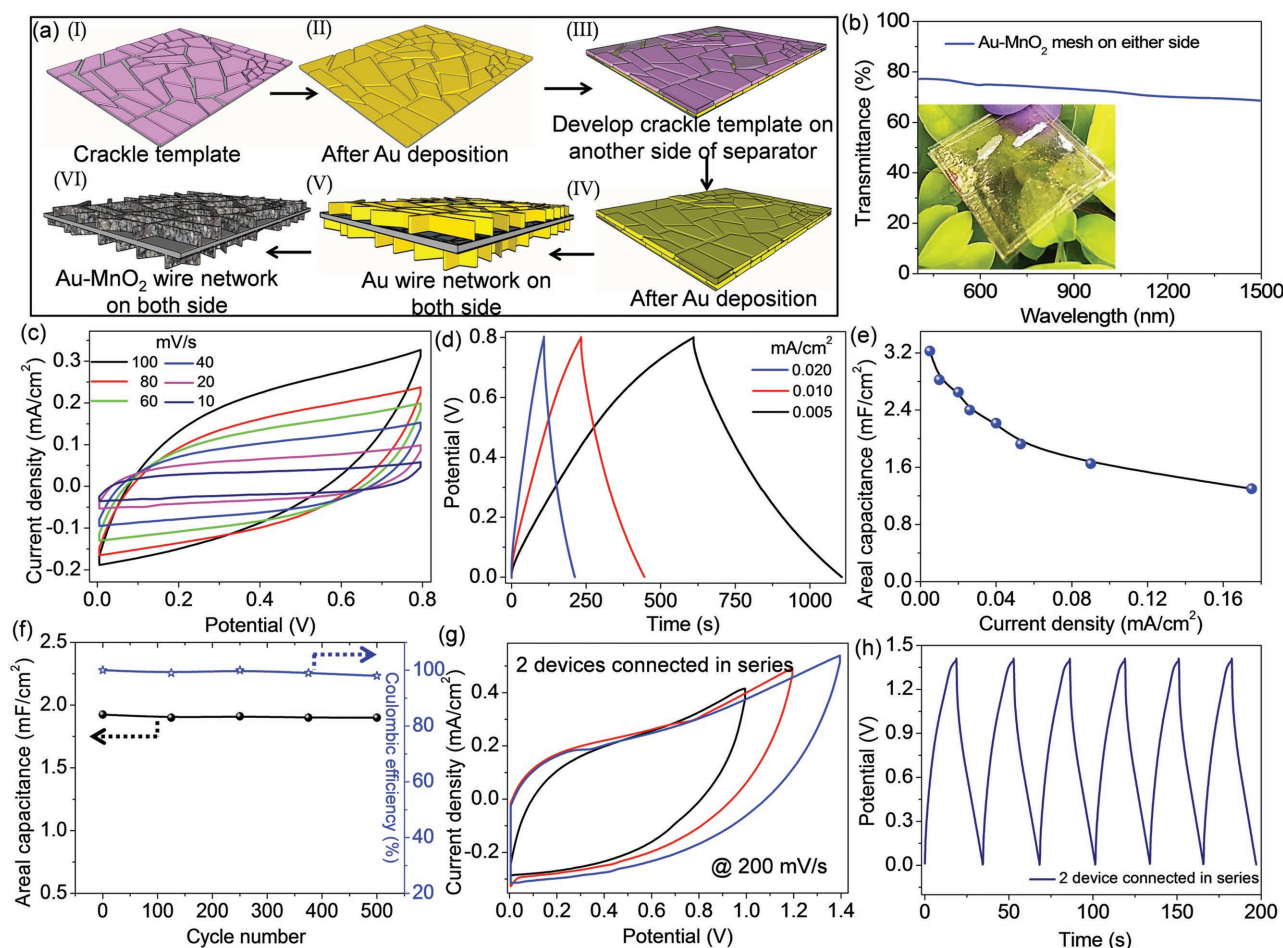


Figure 4. a) Schematic illustration of various steps to fabricate Au/MnO_2 on both sides of the separator. b) Transmittance spectrum of supercapacitor electrodes fabricated on both sides of separator and inset is the photograph of the device. c) CV curves at different scan rates and d) CD curves of Au/MnO_2 (60 min) at various discharge current densities. e) Dependence of areal capacitance on discharging current densities. f) Cycle stability and coulombic efficiency of supercapacitor at a current density of 0.05 mA cm^{-2} . g) CV curves of two devices connected in series at scan rate of 200 mV s^{-1} . h) CD curves of two series-connected devices at 0.27 mA cm^{-2} .

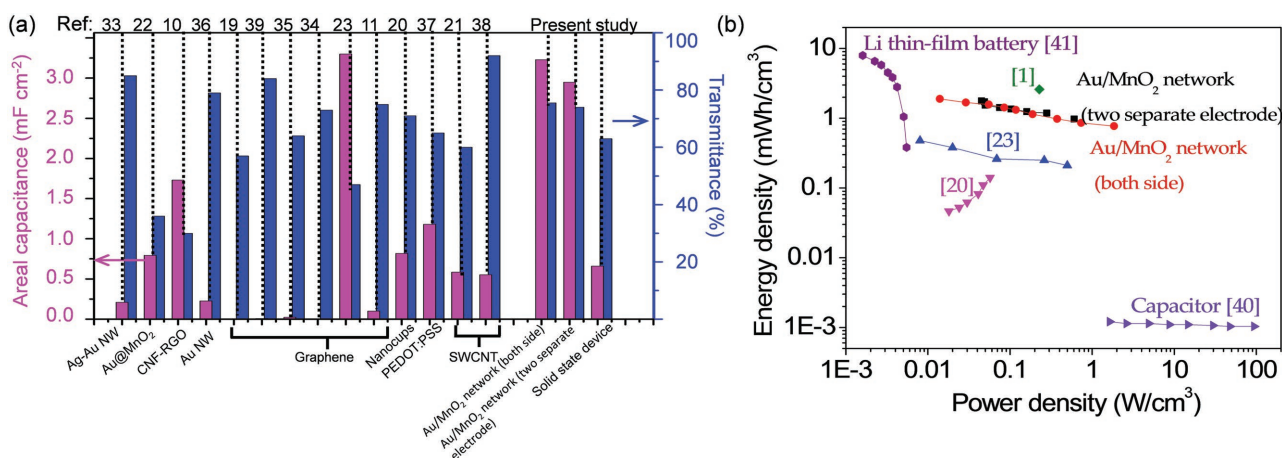


Figure 5. a) Comparing the areal capacitance (two-electrode configuration) and transparency (at 550 nm) of present devices with recent transparent supercapacitor devices. b) Ragone plot comparing the volumetric energy and power densities of devices fabricated in this study with other transparent supercapacitors,^[1,20,23] thin-film batteries,^[41] and capacitors^[40] available in the literature.

was plotted along with the device developed on both sides of the separator in Figure S15 in the Supporting Information. Capacitance values were retained in both the configurations except for slight differences at higher current densities (see Figure S15 in the Supporting Information). Furthermore, these transparent supercapacitors exhibited high stability as their areal capacitance and coulombic efficiency remained unchanged over 500 cycles of CD around 0.05 mA cm⁻². Finally, to demonstrate the potential of Au/MnO₂-based transparent supercapacitor, two devices were connected in series and examined their CV and CD performances. The CV and CD curves clearly show that the potential window of the device was extended up to 1.4 V (Figure 4g,h).

The transparency and electrochemical performance of the present supercapacitors are compared with literature data in **Figure 5a**. It is important to note that the current device besides providing higher transmittance offers higher capacitance as well when compared to literature values (Figure 5a and **Table 1**).^[10,11,19–23,33–39] The energy storage properties of transparent supercapacitor have been evaluated through Ragone plot, in which volumetric energy density was plotted versus power density (Figure 5b). These values were obtained by using the following Equations (3) and (4)^[23]

$$E = \left(\frac{1}{2} \times C \times (\Delta V)^2 \right) / 3600 \quad (3)$$

$$P = (E / \Delta t) \times 3600 \quad (4)$$

where E is the energy density (Wh cm⁻³), C is the volumetric areal capacitance (F cm⁻³), ΔV is the discharge voltage range (V), P is the power density (W cm⁻³) and Δt is the discharge time (s). The data from the present study are compared with high-power electrolytic capacitor (3 V/300 μF),^[40] thin-film lithium-ion batteries^[41] and transparent supercapacitors from literature^[1,20,23] as shown in the Ragone plot (Figure 5b). In comparison to two electrodes separated by a separator, the present configuration with electrodes on either side of the separator has shown slightly higher values. The obtained

density values are an order of magnitude higher than that of the transparent carbon-film-based supercapacitors.^[20] In particular, the obtained energy and power densities of transparent supercapacitor fabricated in this study are highly comparable with those of other transparent supercapacitors^[1,20,23] and Li-thin-film batteries.^[41]

In this study although Au metal is expensive, it was chosen as current collecting electrode mainly due to its stability toward electrochemical environment where metals such as Ag, Cu, etc., fail. This is a matter of concern in all metal-based supercapacitor devices.^[22] As regards MnO₂,

Table 1. Transparency and areal capacitance comparison of devices fabricated in this work with various transparent supercapacitors reported in the literature.

Material	Transmittance @ 550 nm [%]	Areal capacitance [mF cm ⁻²]	Reference
Ag–Au NW	≈85	0.210	[33]
Au/MnO ₂	36	0.795	[22]
CNF-RGO	30	1.730	[10]
Au NW	79	0.227	[36]
Graphene	57	0.006	[19]
Graphene	84	0.008	[39]
Graphene	64	0.025	[35]
Graphene	73	0.005	[34]
Graphene	≈47	3.3	[23]
Graphene	≈75	0.101	[11]
Nanocups	71	0.818	[20]
PEDOT:PSS	65	1.18	[37]
SWCNT	60	0.584	[21]
SWCNT	92	0.552	[38]
Au/MnO ₂ network (both sides)	75.5	3.23	This work
Au/MnO ₂ network (two separate electrode)	74	2.95	This work
Solid-state device	63	0.660	This work

abundance, low cost, environmental benignity as well as high theoretical capacitance (1370 F g^{-1}) makes it ideal for pseudocapacitive active material. The separator used as substrate is transparent, flexible, thin light weight, porous as well as highly stable toward mesh fabrication processes. Furthermore, electrodeposition of MnO_2 on Au mesh transparent current collector not only retains the transparency but also improves its contact (R_s , 32Ω). It may be noted that the Au/ MnO_2 meshes are highly transparent even in the near-IR regions (Figure 2b), unlike ITO or oxide-based devices where electrodes are effectively transparent only in visible region due to electronic absorption of oxides.^[4]

3. Conclusions

In conclusion, highly transparent and flexible supercapacitors employing metal network structure have been fabricated. A core-shell network of Au/ MnO_2 with high transmittance was fabricated through simple crackle template process developed in this laboratory followed by electrodeposition technique. Using the novel approach of fabricating the electrodes on the separator itself, the interaction of electrolyte with active material (MnO_2) was improved which further enhanced the storage capacity along with cycling stability. The resulting supercapacitor yielded the areal capacitance of $\approx 3 \text{ mF cm}^{-2}$ with nearly 75% transmittance at 550 nm. The obtained values are highly comparable with transparent supercapacitors devices fabricated in the recent literature. Further investigation revealed that both the electrodes can be fabricated on either sides of a separator with no loss in transmittance and capacitance. In addition, fabrication cost of the device could be reduced further by using Ag/Au core-shell mesh structures. These fabrication methods can be generalized for the production of large-area transparent devices with networked metal or material of one's desire.

4. Experimental Section

Fabrication of Au Mesh: The fabrication process involves three simple steps. Initially, an acrylic resin-based precursor (0.6 g mL^{-1} , Ming Ni Cosmetics Co., Guangzhou, China) was spin coated over a precleaned and dried separator substrate (BOPP films from Mirwec Film, Inc.) to create a crackle template. By depositing Au over the template through physical evaporation process, followed by removal of the template yields highly interconnected Au wire mesh on the separator substrate.

Fabrication of Au/ MnO_2 Mesh: MnO_2 was electrodeposited over Au mesh by immersing the electrode into plating solution composed of 1:1 mixture of $50 \times 10^{-3} \text{ M Na}_2\text{SO}_4$ and $50 \times 10^{-3} \text{ M Mn}(\text{Ac})_2$ under steady potential of 0.45 V versus Ag/AgCl electrode and Pt as reference electrode. MnO_2 loading was varied with time of deposition (8–90 min).

Fabrication of Solid-State Supercapacitor: PVA/ H_2SO_4 gel was used as an electrolyte as well as a spacer between two Au/ MnO_2 (60 min) electrodes. The gel electrolyte was prepared by dissolving 1 g of H_2SO_4 and 1 g PVA in 10 mL of DI water at 80°C under vigorous stirring till it dissolved completely to form a clear solution.

Characterization: Morphology of crackle template and Au/ MnO_2 mesh were investigated using SEM from Nova NanoSEM 600 instrument (FEI Co., The Netherlands). Energy-dispersive spectroscopy mapping/spectrum of Au/ MnO_2 mesh was carried out using an EDAX Genesis instrument (Mahwah, NJ) attached to the SEM column. TEM measurements were performed with a JEOL-3010 instrument operating at 300 kV. Sheet resistance measurement was performed using 4-point probe Station from Techno Science Instruments, India. Transmittance measurement was carried out using UV-vis spectrophotometer from Perkin-Elmer Model Lambda 900 UV-vis/near-IR spectrophotometer. XPS measurements of Au/ MnO_2 mesh were carried out using Omicron SPHERA spectrometer (Al $K\alpha = 1486.6 \text{ eV}$). Atomic force microscopic (AFM) imaging was done using a dilInnova SPM (Veeco, USA) with Si probes (model, RTESPA, spring constant 40 N m^{-1}) in tapping mode. Electrochemical performance of Au/ MnO_2 was measured using CH Instruments 650 Electrochemical Station (Austin, TX, USA).

Supporting Information

Supporting Information is available from the Wiley Online Library or from the author.

Acknowledgements

The authors thank Prof. C. N. R. Rao for his encouragement. The financial support from DST, India, is gratefully acknowledged. S.K. and C.S. acknowledge JNCASR & IGSTC and UGC, respectively, for their fellowships.

Conflict of Interest

The authors declare no conflict of interest.

- [1] Z. S. Wu, K. Parvez, X. Feng, K. Müllen, *Nat. Commun.* **2013**, *4*, 2487.
- [2] L. Xingyou, H. Akihiko, F. Takeshi, C. Mingwei, *Nat. Nanotechnol.* **2011**, *6*, 232.
- [3] C. Liu, L. Feng, M. Lai-Peng, C. Hui-Ming, *Adv. Mater.* **2010**, *22*, 4647.
- [4] Y. Hu, H. Zhu, J. Wang, Z. Chen, *J. Alloys Compd.* **2011**, *509*, 10234.
- [5] P. Tang, L. Han, L. Zhang, *ACS Appl. Mater. Interfaces* **2014**, *6*, 10506.
- [6] S. Li, D. Huang, B. Zhang, X. Xu, M. Wang, G. Yang, Y. Shen, *Adv. Energy Mater.* **2014**, *4*, 1301655.
- [7] L. Hu, H. Wu, Y. Cui, *Appl. Phys. Lett.* **2010**, *96*, 183502.
- [8] S. Hu, R. Rajamani, X. Yu, *Appl. Phys. Lett.* **2012**, *100*, 104103.
- [9] G. Zheng, L. Hu, H. Wu, X. Xie, Y. Cui, *Energy Environ. Sci.* **2011**, *4*, 3368.
- [10] K. Gao, Z. Shao, X. Wu, X. Wang, Y. Zhang, W. Wang, F. Wang, *Nanoscale* **2013**, *5*, 5307.
- [11] K. Jo, S. Lee, S. M. Kim, J. B. In, S. M. Lee, J. H. Kim, H. J. Lee, K. S. Kim, *Chem. Mater.* **2015**, *27*, 3621.

- [12] R. Gupta, K. D. M. Rao, G. U. Kulkarni, *RSC Adv.* **2015**, *8*, 60.
- [13] G. Cai, P. Darmawan, M. Cui, J. Wang, J. Chen, S. Magdassi, P. S. Lee, *Adv. Energy Mater.* **2016**, *6*, 1501882.
- [14] D. S. Hecht, L. Hu, G. Irvin, *Adv. Mater.* **2011**, *23*, 1482.
- [15] G. U. Kulkarni, S. Kiruthika, R. Gupta, K. D. M. Rao, *Curr. Opin. Chem. Eng.* **2015**, *8*, 60.
- [16] T. Sannicolo, M. Lagrange, A. Cabos, C. Celle, J. P. Simonato, D. Bellet, *Small* **2016**, *12*, 6052.
- [17] S. Ye, A. R. Rathmell, Z. Chen, I. E. Stewart, B. J. Wiley, *Adv. Mater.* **2014**, *26*, 6670.
- [18] Z. Yin, J. Zhu, Q. He, X. Cao, C. Tan, H. Chen, Q. Yan, H. Zhang, *Adv. Energy Mater.* **2014**, *4*, 1300574.
- [19] T. Chen, Y. Xue, A. K. Roy, L. Dai, *ACS Nano* **2013**, *8*, 1039.
- [20] H. Y. Jung, M. B. Karimi, M. G. Hahm, P. M. Ajayan, Y. J. Jung, *Sci. Rep.* **2012**, *2*, 773.
- [21] Z. Niu, W. Zhou, J. Chen, G. Feng, H. Li, Y. Hu, W. Ma, H. Dong, J. Li, S. Xie, *Small* **2013**, *9*, 518.
- [22] T. Qiu, B. Luo, M. Giersig, E. M. Akinoglu, L. Hao, X. Wang, L. Shi, M. Jin, L. Zhi, *Small* **2014**, *10*, 4136.
- [23] N. Li, G. Yang, Y. Sun, H. Song, H. Cui, G. Yang, C. Wang, *Nano Lett.* **2015**, *15*, 3195.
- [24] R. Gupta, K. D. M. Rao, K. Srivastava, A. Kumar, S. Kiruthika, G. U. Kulkarni, *ACS Appl. Mater. Interfaces* **2014**, *6*, 13688.
- [25] S. Kiruthika, R. Gupta, K. D. M. Rao, S. Chakraborty, N. Padmavathy, G. U. Kulkarni, *J. Mater. Chem. C* **2014**, *2*, 2089.
- [26] S. Kiruthika, S. Singh, G. U. Kulkarni, *RSC Adv.* **2016**, *6*, 44668.
- [27] K. D. M. Rao, R. Gupta, G. U. Kulkarni, *Adv. Mater. Interfaces* **2014**, *1*, 1400090.
- [28] R. Gupta, K. D. M. Rao, S. Kiruthika, G. U. Kulkarni, *ACS Appl. Mater. Interfaces* **2016**, *8*, 23419.
- [29] S. Kiruthika, R. Gupta, A. Anand, A. Kumar, G. U. Kulkarni, *ACS Appl. Mater. Interfaces* **2015**, *7*, 27215.
- [30] K. D. M. Rao, G. U. Kulkarni, *Nanoscale* **2014**, *6*, 5645.
- [31] R. B. Rakhi, W. Chen, D. Cha, H. N. Alshareef, *Adv. Energy Mater.* **2012**, *2*, 381.
- [32] P. Lv, P. Zhang, Y. Feng, Y. Li, W. Feng, *Electrochim. Acta* **2012**, *78*, 515.
- [33] H. Lee, S. Hong, J. Lee, Y. D. Suh, J. Kwon, H. Moon, H. Kim, J. Yeo, S. H. Ko, *ACS Appl. Mater. Interfaces* **2016**, *8*, 18516.
- [34] P. Xu, J. Kang, J. B. Choi, J. Suhr, J. Yu, F. Li, J. H. Byun, B. S. Kim, T. W. Chou, *ACS Nano* **2014**, *8*, 9437.
- [35] Y. Gao, Y. S. Zhou, W. Xiong, L. J. Jiang, M. Mahjouri-samani, P. Thirugnanam, X. Huang, M. M. Wang, L. Jiang, Y. F. Lu, *APL Mater.* **2013**, *1*, 012101.
- [36] S. Gong, Y. Zhao, Q. Shi, Y. Wang, L. W. Yap, W. Cheng, *Electroanalysis* **2013**, *1*, 012101.
- [37] T. Cheng, Y. Z. Zhang, J. D. Zhang, W. Y. Lai, W. Huang, *J. Mater. Chem. A* **2016**, *4*, 10493.
- [38] K. Petri, L. Nguyen Dang, S. Le Hoang, V. A. Ilya, T. Alexey, S. I. Jukka, G. N. Albert, K. Tanja, *Nanotechnology*, **2016**, *27*, 235403.
- [39] X. Fan, T. Chen, L. Dai, *RSC Adv.* **2014**, *4*, 36996.
- [40] M. F. El-Kady, V. Strong, S. Dubin, R. B. Kaner, *Science* **2012**, *335*, 1326.
- [41] D. Pech, M. Brunet, H. Durou, P. Huang, V. Mochalin, Y. Gogotsi, P. L. Taberna, P. Simon, *Nat. Nanotechnol.* **2010**, *5*, 651.

Received: June 6, 2017
Revised: July 19, 2017
Published online: August 21, 2017